A passive fathometer technique for imaging seabed layering using ambient noise

Martin Siderius
HLS Research Inc., 12730 High Bluff Drive, Suite 130, San Diego, California 92130

Chris H. Harrison
NATO Undersea Research Centre, Viale S. Bartolomeo 400, 19138 La Spezia, Italy

Michael B. Porter
HLS Research Inc., 12730 High Bluff Drive, Suite 130, San Diego, California 92130

A passive acoustics method is presented that uses the ocean ambient noise field to determine water depth and seabed sub-bottom layering. Correlating the noise field measured by two sensors one can recover a function that closely resembles the two-point Green's function representing the impulse response between the two sensors. Here, a technique is described that is based on noise correlations and produces what is effectively a passive fathometer that can also be used to identify sub-bottom layers. In principle, just one or two hydrophones are needed—given enough averaging time. However, by combining the cross correlations of all hydrophone pairs in a vertical array a stronger signature can be obtained and this greatly reduces averaging time. With a moving (e.g., drifting) vertical array, the resulting algorithm yields both a map of the bottom depth (passive fathometer) and the locations of significant reflectors in the ocean sub-bottom. In this paper, the technique is described and illustrated using numerical simulations. Results are also shown from two experiments. In the first, ambient noise is taken on a fixed array in the 200–1500 Hz frequency band and the second experiment uses a drifting array in the 50–4000 Hz band. © *2006 Acoustical Society of America.* [DOI: 10.1121/1.2227371]

I. INTRODUCTION

Passive techniques that exploit the ocean ambient noise field are useful when active sonar is not practical or feasible. Situations include operations in areas where sonar is prohibited due to, for example, environmental restrictions. In this paper, a technique is described that uses ambient noise correlations to determine the acoustic travel time from hydrophones in the water column to the seabed. This provides a measure of the absolute depth of both the water-sediment interface (a fathometer) and the sub-bottom layers. Vertical beamforming is used to limit the contributions from distant noise sources while emphasizing those directly overhead; this greatly reduces the averaging time required to extract coherent arrivals. A simplified derivation of the noise correlation function is included to illustrate how coherent arrivals from the noise field are used for the passive fathometer processing.

In recent years, several new techniques have been proposed to exploit the ocean ambient noise field for sonar and seismic applications. Harrison and Simons showed that the ratio of the upward to downward directionality of the noise field is the incoherent bottom reflection coefficient, and they measured it by beamforming on a vertical array.[1] That technique was extended to derive sub-bottom layering with a drifting array by reconstructing the reflection loss phase using spectral factorization.[2,3] Roux, Kuperman, and the NPAL Group demonstrated how wave fronts can be extracted from the ocean noise field using horizontally separated hydrophones.[4] Their work was inspired by the developments by Weaver and Lobkis[5] and the conjecture put forward by Rickett and Claerbout:[6] "By cross correlating noise traces recorded at two locations on the surface, we can construct the wave field that would be recorded at one of the locations if there was a source at the other." The wave fronts reconstructed by Roux, Kuperman, and the NPAL Group showed that, in fact, cross correlations between two receivers resembled that from a directional source to a receiver with the directionality dependent on the characteristics of the noise sources. A more detailed derivation of the angularly shaded, two-point Green's function obtained from ocean noise correlation functions was developed by Sabra *et al.*[7] In that paper it was shown that the coherent arrivals are primarily due to the noise sources located in the end fire direction to the hydrophones being cross correlated. Given sufficient averaging time, the cross correlation produces the eigenray arrivals between the two hydrophones.

The work described here exploits the same noise cross-correlation phenomenon. However, closely spaced hydrophones vertically separated are used to take advantage of both cross correlations between sensors and beamforming. This allows for short averaging times, on the order of 30 s, to extract the coherent arrivals. This combination makes it possible to estimate both the water depth and sub-bottom layering from the ambient noise correlation function. In Sec. II, a simplified theoretical description is developed that includes a method of images construction to elucidate the nature of arrivals that are extracted from the noise correlation function.
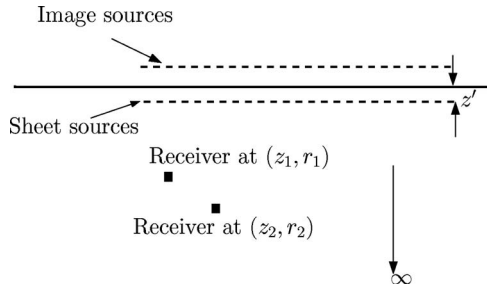
FIG. 1. Geometry for the half-space problem where the perfectly reflecting surface gives rise to image sources at $z=-z'$.

In Sec. III, numerical simulations illustrate the technique under known conditions. Finally, in Sec. IV results are shown from experiments using a fixed vertical array and a drifting vertical array.

II. THEORETICAL DESCRIPTION

Over the last several decades, a number of theoretical approaches have been developed to describe the ocean ambient noise field. In Buckingham,[8] a normal mode approach was used to develop a model for ambient noise in shallow water waveguides. Harrison[9] developed a ray-based approach which is particularly advantageous for broadband computations and for higher frequencies. Here, the wave approach taken by Kuperman and Ingenito[10] is adopted. This approach is used together with the method of images to construct the Green's functions and is similar to that taken by Sabra *et al.*[7] The special geometry of vertically separated receivers used for the passive fathometer processing simplifies the analysis that is presented here. The purpose of these derivations is to demonstrate, for geometries that can be easily treated analytically, how the noise correlations between two receivers can closely resemble the response from a source to receiver.

The sound generated from wind action on the surface is modeled as an infinite sheet of point sources located just below the surface at depth z'. The geometry for the sheet source and receivers is shown in Fig. 1. The derivation and notation follows Refs. 10 and 11. To start, (assuming cylindrical symmetry) the cross spectral density is written as an integral over all source directions,

$$C(\omega,R,z_1,z_2) = \frac{8\pi^2 q^2}{k^2(z')}$$
$$\times \int_0^\infty [g(k_r,z_1,z')g^*(k_r,z_2,z')]J_0(k_rR)k_rdk_r.$$

(1)

This derived cross-spectral density $C(\omega)$ (at frequency ω), between receivers at depths z_1 and z_2 is written in terms of the (range-independent) Green's functions with horizontal wave-number k_r (the * indicates the complex conjugation), $k=\omega/c_w$, and water sound speed c_w. The quantity q is included to give proper scaling due, for instance, to various wind speeds. The Bessel function (J_0) is required for receivers separated in range by $R=r_1-r_2$. For the vertically sepa-

rated receivers used for the passive fathometer process $J_0(k_rR)=1$.

It is worthwhile to note the similarity in form between the cross-spectral density (1) and the pressure field from a point source at z_1 to a receiver at depth z_2

$$P(\omega,R,z_1,z_2) = \int_0^\infty g(k_r,z_1,z_2)J_0(k_rR)k_rdk_r.$$

(2)

The integral in Eq. (2) produces the usual pressure field as a function of range and depth due to a point source. Wave-number integration methods have been developed which evaluate this integral and are described in Refs. 11–13. An important difference between Eqs. (1) and (2) is that the cross-spectral density is an ensemble average and the pressure field is deterministic. With measured data, the averaging time needed can be an important consideration for noise processing techniques.

A. Calculating the Green's function using the method of images

The similarity between Eqs. (1) and (2) depends on the extent to which the product of Green's functions in Eq. (1) behaves like the single Green's function in Eq. (2). That is, to what extent does the noise correlation behave as a source-receiver pair? To gain insight into this question it is worthwhile to begin with simple Green's functions constructed using the method of images.

The environment is assumed to be a fluid halfspace (i.e., no seabed) with the noise source located at z'. The pressure release surface gives rise to a sheet source of images at $-z'$. The geometry is shown in Fig. 1.

The Green's function to the receiver at z_1 from sources at z' and its image at $-z'$ can be written in terms of the horizontal wave-number k_r

$$g(k_r,z_1,z') = \left[\frac{e^{ik_z|z_1-z'|}}{4\pi ik_z} - \frac{e^{ik_z(z_1+z')}}{4\pi ik_z}\right],$$

(3)

where the vertical wave number is defined as $k_z=\sqrt{k^2-k_r^2}$. Since the sound sources are very near the surface (within a fraction of a wavelength) the receivers can safely be assumed deeper and the magnitude sign in the exponential can be omitted. Denoting $g_1=g(k_r,z_1,z')$ and $g_2=g(k_r,z_2,z')$, the term in square brackets in Eq. (1) is

$$g_1g_2^* = \left[\frac{e^{ik_z(z_1-z')}}{4\pi ik_z} - \frac{e^{ik_z(z_1+z')}}{4\pi ik_z}\right]$$
$$\times \left[\frac{e^{ik_z(z_2-z')}}{4\pi ik_z} - \frac{e^{ik_z(z_2+z')}}{4\pi ik_z}\right]^*.$$

(4)

After some manipulation this can be written

$$g_1g_2^* = \frac{1}{(2\pi|k_z|)^2}[e^{i(k_zz_1-k_z^*z_2)}\sin(k_zz')\sin(k_z^*z')].$$

(5)

This is the result for the most common case of a surface of dipole sources (monopoles very near the pressure release sur-
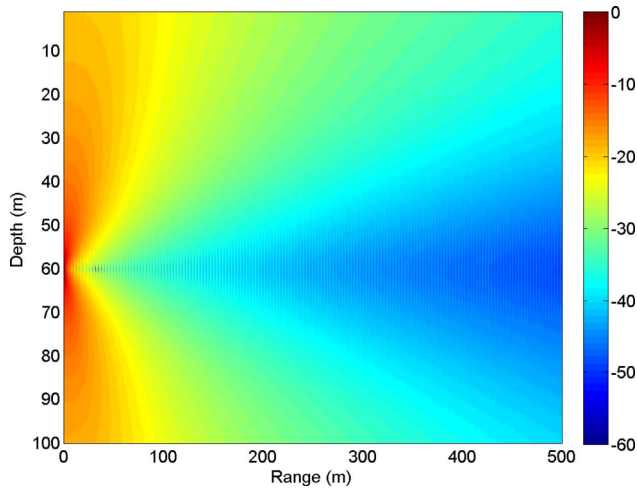
FIG. 2. Cross spectral density, normalized on a decibel scale $[10 \log C(\omega)]$ given by Eq. (6). The source appears to be at the location of the receiver at z_1 but is not a point source but has dipole-like shading.

face). This is essentially the result obtained by Cron and Sherman[14] for the deep ocean with limited seabed reflections (the equivalence of this form to the earlier work was derived by Kuperman and Ingenito).[10] The cross-spectral density is written considering only real k_z

$$
C(\omega, R, z_1, z_2) = \frac{2q^2}{k^2(z')}
$$
$$
\times \int_0^k \left[\frac{e^{ik_z(z_1-z_2)}\sin^2(k_z z')}{|k_z|^2} \right] J_0(k_r R) k_r dk_r.
\tag{6}
$$

The term in square brackets looks similar to a single, free-space Green's function but *not* originating from a surface source but rather for a source located at z_1 and received at z_2. Further, rather than a true, free-space Green's function there is an extra $\sin^2(k_z z')$ term that gives a dipole-like shading. The cross-spectral density is, therefore, expected to look similar to the pressure field from a shaded free-space point source. A plot of the cross-spectral density given by Eq. (6) is shown in Fig. 2. In the figure, the first noise receiver is fixed at $z_1=60$ m, $r_1=0$ m and this is correlated with receivers at $z_2=0-100$ m, $r_2=0-500$ m (for 500 Hz), note that the source *appears* at (z_1, r_1).

In the previous description k_z was assumed real which makes the expression easier to interpret but is only correct for $k_r < k$. This is only a minor approximation since there is an exponential decay that occurs for $k_r > k$ (i.e., the evanescent part of the wave-number spectrum). Consider expanding the first term in square brackets in Eq. (5)

$$
e^{i(k_z z_1 - k_z^* z_2)} = e^{i\Re\{k_z\}(z_1-z_2)} \times e^{-\Im\{k_z\}(z_1+z_2)},
\tag{7}
$$

where $\Re\{k_z\}$ and $\Im\{k_z\}$ indicate the real and imaginary components of k_z. This indicates that for the part of the wave-number spectrum where k_z has an imaginary component $g_1 g_2^*$ will decay exponentially in depth.

Next, the surface and bottom boundaries are included. This will result in an infinite number of image sources, however to show the pattern and for illustration purposes, just a
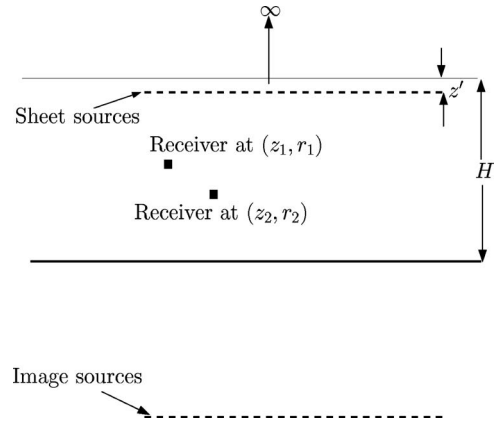

FIG. 3. Geometry for the half-space problem where the reflecting bottom gives rise to image sources at $z=2H-z'$ in addition to the surface image.

single bottom image and a single surface image are included in this discussion. The geometry is shown in Fig. 3 for a water depth of H. Including the first bottom image yields a superposition of the source at z' and the image at $2H-z'$, that is

$$
g_1 = \left[\frac{e^{ik_z(z_1-z')}}{4\pi i k_z} - \frac{e^{ik_z[(H-z_1)+(H-z')]}}{4\pi i k_z} \right].
\tag{8}
$$

Similarly for g_2

$$
g_2 = \left[\frac{e^{ik_z(z_2-z')}}{4\pi i k_z} - \frac{e^{ik_z[(H-z_2)+(H-z')]}}{4\pi i k_z} \right].
\tag{9}
$$

The product $g_1 g_2^*$ is

$$
g_1 g_2^* = \frac{2}{(4\pi|k_z|)^2}\{\cos[k_z(z_1-z_2)] - \cos(k_z[(H-z_1)
$$
$$
+ (H-z_2)])\}.
\tag{10}
$$

The first term in square brackets looks like a point source term between z_1 and z_2. The second term looks similar to an image source from the bottom bounce.

Including both the images from the bottom and the surface, the receiver at z_1 has a Green's function

$$
g_1 = \left[\frac{e^{ik_z(z_1-z')}}{4\pi i k_z} - \frac{e^{ik_z(z_1+z')}}{4\pi i k_z} - \frac{e^{ik_z[(H-z_1)+(H-z')]}}{4\pi i k_z} \right].
\tag{11}
$$

Similarly, the Green's function at z_2

$$
g_2 = \left[\frac{e^{ik_z(z_2-z')}}{4\pi i k_z} - \frac{e^{ik_z(z_2+z')}}{4\pi i k_z} - \frac{e^{ik_z[(H-z_2)+(H-z')]}}{4\pi i k_z} \right].
\tag{12}
$$

The product $g_1 g_2^*$ is

$$
g_1 g_2^* = \frac{1}{(2\pi|k_z|)^2}\left\{ e^{ik_z(z_1-z_2)}\sin^2(k_z z') + \frac{1}{4}e^{-ik_z(z_1-z_2)} \right.
$$
$$
- \frac{1}{2}\cos(k_z[(H-z_1)+(H-z_2)])
$$
$$
\left. + \frac{1}{2}\cos(k_z[(H-z_1)+(H-z_2)-2z']) \right\}.
\tag{13}
$$

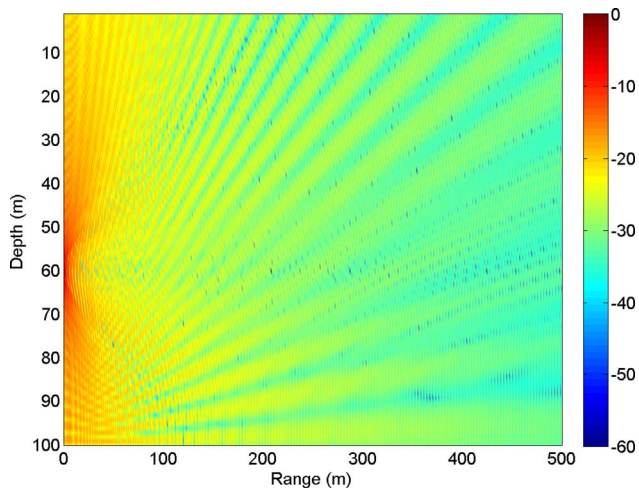This is a fairly complicated expression, but the first two

FIG. 4. Cross spectral density, normalized on a decibel scale $[10 \log C(\omega)]$ for the case of perfectly reflecting boundaries (including just the first bottom and surface images). The source appears to be at the location of the receiver at z_1 along with an image giving rise to the inverted Lloyd mirror pattern.
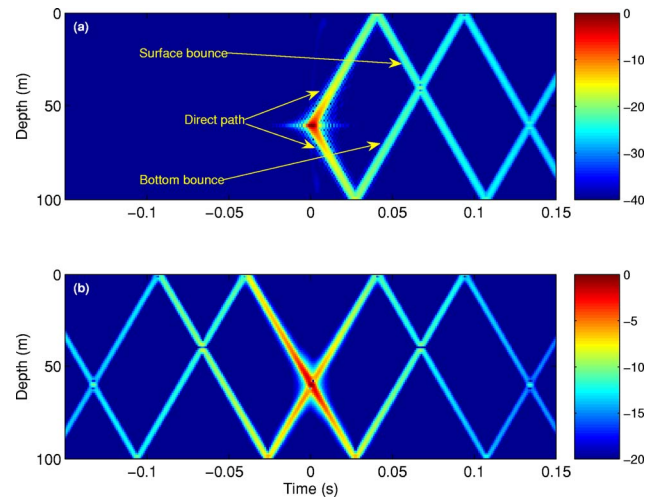

FIG. 5. Panel (a) shows the response on a 100-m vertical array from a point source at 60-m depth (all colocated in range). In panel (b) the noise cross correlations are shown using the reference phone at 60 m correlated with the other hydrophones in the array. The negative part of the time series is due to the cross-correlation process. In both (a) and (b) the envelope of the response is normalized and put on a decibel scale.

terms in curly brackets correspond to the shaded point source between z_1 and z_2. The last two terms correspond to an image of the dipolelike "source" (i.e., the bottom bounce). In other words, to the receiver at z_2 it appears like a shaded source at z_1 and a bottom bounce image. When processing for bottom depth and sub-bottom layering, however, the source directionality will have very little impact since the interest is in the vertically received bottom bounces. Inserting Eq. (13) into Eq. (1) the field can be calculated and this is shown in Fig. 4 for $z_1 = 60$ m and frequency of 500 Hz. The figure is consistent with the terms in Eq. (13) with the appearance of an inverted Lloyd mirror pattern.[11] Note that for the derivation, k_z is assumed real but for the numerical simulation results shown in Fig. 4, the complex values are included. Numerically, it is not difficult to include the higher order images (i.e., use the complete Green's functions) and this will be done for the time-domain solutions in the following sections.

III. TIME-DOMAIN PROCESSING FOR THE PASSIVE FATHOMETER

Next, consider the cross-spectral density in the time domain where the fathometer and sub-bottom profiler are most useful. Using Fourier synthesis, the frequency domain solution is transformed to the time-domain τ according to

$$c(\tau, z_1, z_2) = \frac{1}{2\pi} \int_{-\infty}^{\infty} C(\omega, z_1, z_2) e^{-i\omega\tau} d\omega. \quad (14)$$

Using the synthesis Eq. (14), the frequency domain correlation of the ambient noise field between two (vertically separated) receivers at z_1 and z_2 is transformed to a time series. Note that with vertically separated receivers there is no R dependency and the Bessel function in Eq. (1) disappears. According to the previous analysis this is expected to look similar to a source at z_1 and a receiver at z_2 with some slight differences in the source directionality as described.

To illustrate, consider a vertical array in a water depth of $H = 100$ m with perfectly reflecting boundaries. The array

spans the water column with receivers every meter from 1 to 100 m. To orient the reader, the response on the array due to a true point source located at 60-m depth is shown in panel (a) of Fig. 5. The vertical array and source are all colocated at range 0. The time-domain signal is generated by computing the response from 1 to 512 Hz with 1 Hz sampling and using Fourier synthesis to produce a 1 s time series at each receiver. A Hanning window is applied to the spectrum before transforming in order to reduce time-domain ringing. The direct paths are those that reach the receivers first and are indicated in the figure. Arriving later in time are the bottom and surface bounces that are also indicated. In panel (b) of Fig. 5, the noise cross-correlation time-domain responses are shown. The reference hydrophone z_1 is at 60 m depth and cross correlated with the other receivers in the array. That is, the cross-spectral density is formed between z_1 and all the other receivers at each frequency (from 1 to 512 Hz with 1 Hz sampling). Fourier synthesis is used in exactly the same way as for the true source to produce a 1 s time series at each receiver. For the fathometer application, the interest is in arrival times, and for this the two signals in panels (a) and (b) of Fig. 5 are practically the same for positive time.

Some differences between the cross-correlation time series and that from a true source become evident when a more realistic seabed is substituted for the perfectly reflecting bottom boundary. These differences will not impact the processing for bottom depth and layering as will be demonstrated in the next sections with simulations and data. However, it is important to note these differences to explain some of the features that appear in the intermediate results. The simulation will use the same geometry as for the perfectly reflecting boundaries of Fig. 5 but with an acoustic half-space seabed with 1550 m/s sound speed, density of 1.5 g/cm³, and attenuation of 0.2 dB/λ (decibels per wavelength). The Green's functions and integral in Eq. (1) are evaluated using the OASES program.[12,15] In panel (a) of Fig. 6 it can be seen

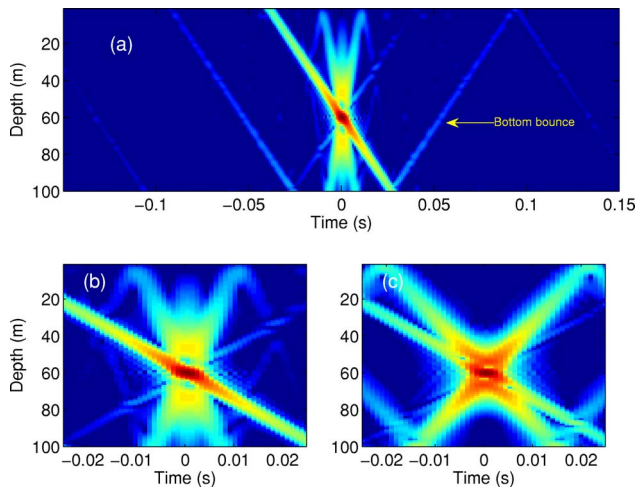Siderius *et al.*: Passive fathometer

FIG. 6. In panel (a) a realistic (lossy) seabed is used with the same geometry as for panel (b) of Fig. 5. Note, the wavefronts near time-lag zero are propagating at a more horizontal angle relative to the bottom bounce (the M-shape near time zero). In panel (b) is a zoom of (a) showing the details of the wavefront. The propagation angle of the wavefront in (b) corresponds to the critical angle of the seabed. In (c) the seabed sound speed is changed to 1750 m/s and the steeper propagation angle of the wavefront near time-lag zero can be seen.

that the bottom bounce is similar to the case of the perfectly reflecting boundary with the exception of the higher loss on the bottom bounce. One of the differences with this simulation occurs near time lag zero. A zoomed in display in panel (b) shows a wave front arriving more horizontally than the bottom bounce (the M-shape near time zero). The angle of this wave front corresponds to the critical angle of the 1550 m/s seabed. To compare, in panel (c) the seabed sound speed is changed to 1750 m/s and the angle of the wave front has increased. These wave fronts that occur at the critical angle suggest this process is detecting the head wave. These wave fronts, near time-lag zero, are at angles that are different from the bottom bounce and will have insignificant impact on the passive fathometer processing. They may,

however, be important for identifying the critical angle of the seabed if they can also be detected using measured data. They will not be considered further in this paper as the focus is on the bottom and sub-bottom returns.

In addition to the wave fronts arriving near time lag zero there are additional features that also occur near time-lag zero. These too, will also have a negligible effect on the final passive fathometer processing but help in identifying features that can be seen in some of the intermediate results. To understand, consider a coherent "click" (or impulse) generated on the surface from various noise events. Again, take the reference receiver $z_{Ref}=60$ m and two separate receivers $z_1=25$ m and $z_2=95$ m. These coherent sounds will have a direct arrival on each receiver followed by bottom and sub-bottom arrivals (bounces from the seabed). The timing of these impulses depends on receiver depth and are shown in Fig. 7. Since z_1 is above the reference, the correlation of the two for positive lag time (indicated in the figure as $z_{Ref}*z_1$) shows the initial weak arrivals followed later by a perfect reproduction of the bottom and sub-bottom arrivals. For $z_{Ref}*z_2$, the positive lags show the perfect reproduction of the impulses received on z_2 (no faint arrivals). The main point is that regardless of the relative position of the receiver, the correlation processing produces the coherent bottom and sub-bottom arrivals. There can be a complicated pattern near time-lag zero that includes these weaker direct path and other echoes but these will be of no consequence in the processing as will be described in the next section.

A. Processing vertically separated hydrophones for bottom depth and sub-bottom layering

The previous sections outlined what is expected when the measured noise is correlated between two hydrophones and is transformed into the time domain. The resulting time series is very similar to what is produced from fathometers and sub-bottom profiling sonar systems. That is, a monostatic source/receiver pair. As mentioned, there are some differ-
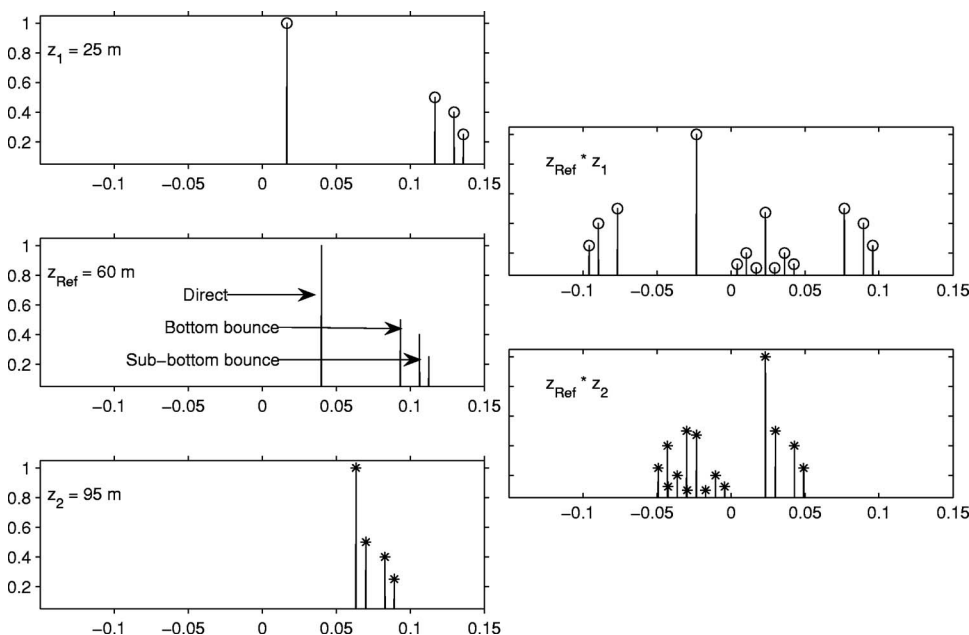

FIG. 7. The impulses received from a coherent "click" from the surface. On the left the received impulses are shown for receivers $z_1=25$ m (top left), $z_{Ref}=60$ m (middle left), and $z_2=95$ m (bottom left). The right side shows the correlation of the reference with the other two channels, $z_{Ref}*z_1$ (top right) and $z_{Ref}*z_2$ (bottom right). Considering only positive time, the receiver above the reference shows faint arrivals before reproducing the bottom and sub-bottom returns. The receiver below the reference shows a perfect reproduction of the bottom and sub-bottom returns without the faint arrivals.

ences between a true source/receiver and the noise correlation processing. The noise correlation processing produces a time series with some directionality and there are arrivals before time-lag zero. Another difference includes arrivals near time-lag zero due to a variety of effects as described previously. However none of these have a significant impact on the ambient noise fathometer/sub-bottom profiler. The only caveat is that the time-series synthesis must be long enough to prevent wrap around. The time series length is set by the selected frequency sampling in the cross-spectral density and, in practice, can be set arbitrarily small.

Next, consider a more realistic simulation consisting of a layered seabed and a realistic array which will be used for the beam-forming part of the processing. The array has the same characteristics as one that is used for the measured data analysis in Sec. IV and has 32 vertically separated hydrophones located between depths of 70 to 75.58 m (0.18 m spacing). The seabed is made up of a top 10 m layer with sound speed of 1550 m/s, density of 1.5 g/cm^3, and attenuation of 0.06 dB/λ. Below that is a 5 m layer with sound speed of 1600 m/s, density of 1.65 g/cm^3, and attenuation of 0.2 dB/λ. The half-space below both sediment layers has sound speed of 1700 m/s, density of 1.65 g/cm^3, and attenuation of 0.2 dB/λ. To simulate the noise field, Eq. (1) is evaluated using the OASES program.[12,15]

The first fathometer processing step is to correlate each receiver in the array with each of the others to form the cross-spectral density at all frequencies (in this simulation frequencies between 50 and 4000 Hz are included). The time series is derived from the frequency domain correlation between receivers at z_n and z_m using Eq. (14). The bottom bounce absolute travel times will correspond to the travel time from the reference receiver to the seabed plus the travel time back to each of the other receivers in the array. Regardless of the receiver chosen as the reference the bottom bounce arrivals will appear delayed from the bottom of the array to the top. These arrivals can all be combined by applying the correct time delay to align the receptions. The alignment is accomplished through delay and sum beam-forming (in the end-fire direction)

$$\widetilde{C}_n(\tau) = \frac{1}{M} \sum_{m=0}^{M-1} C(\tau + m\Delta\tau, z_n, z_m), \tag{15}$$

where

$$\Delta\tau = \frac{\Delta z_h}{c_w}. \tag{16}$$

The time delay between receivers is $\Delta\tau$ and Δz_h is the receiver separation and c_w is the water sound speed.

With receiver 1 (shallowest at 70 m) as the reference, the first bottom reflection arrives on channel 32 (at depth 75.58 m) at time

$$\frac{(100-70)+(100-75.58)}{1500} = 0.0363 \text{ s,} \tag{17}$$

and arrives at channel 1 at 0.04 s. The 32 channels are combined with the appropriate delay to form a single time trace. Next, channel 2 is used as the reference and the 32
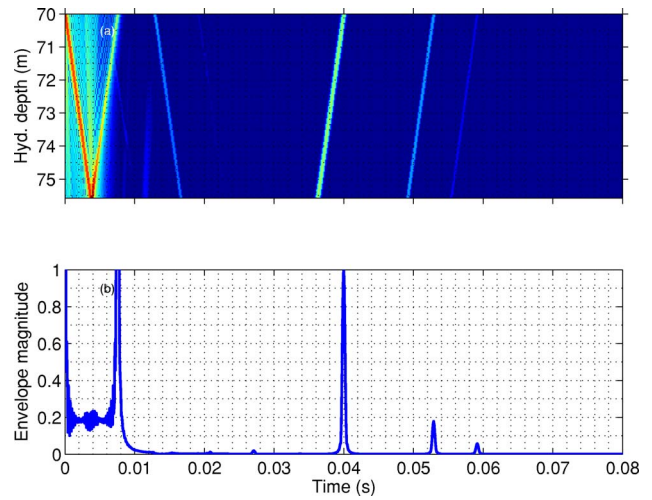

FIG. 8. Panel (a): Stacked, delay, and sum beamforming [i.e., $\widetilde{C}_n(t)$ with $n=1\cdots32$]. Note, there is a bottom reflection corresponding to the water-seabed interface and two sub-bottom reflections corresponding to the two layers. Time series magnitudes are shown on a decibel scale with a range of 30 dB. Panel (b): the second stage of beamforming [i.e., beamforming the sequences shown in panel (a) and given by the expression for $r(t)$]. This is on a normalized linear scale where the envelope has been taken.

receivers are beamformed again. Since channel 2 is the reference, the bottom bounce arrivals arrive earlier by $\Delta\tau$ (since the effective source is now closer to the seabed). The process is repeated until 32 time traces are formed. This first stage of beamforming produces an arrival structure for each reference hydrophone $n=1\cdots32$ and is illustrated in panel (a) of Fig. 8. In panel (a) each row is the result using a different reference channel which causes the delayed arrivals from the seabed. The bottom and sub-bottom reflections are visible with travel times relative n $=1$ (receiver at 70 m depth) since all beamforming is done relative to this receiver.

The time series shown in panel (a) of Fig. 8 is combined again using delay and sum beamforming. This final step aligns the bottom and sub-bottom arrivals into a single time series $r(\tau)$

$$r(\tau) = \frac{1}{N} \sum_{n=0}^{N-1} \widetilde{C}_n(\tau + n\Delta\tau). \tag{18}$$

This is shown in panel (b) of Fig. 8 where the bottom and sub-bottom returns are clearly visible. The absolute water depth can be determined from the two-way travel times taken from depth of receiver $n=1$. In this case the first arrival is at 0.04 s corresponding to $(30\times2)/1500$ s. The sub-bottom layers are also two-way travel times relative to the previous bottom reflection. The next arrival occurs after an additional $(10\times2)/1550$ s, or at 0.0529 s. The final arrival is later by and additional $(5\times2)/1600$ s, or at 0.0592 s. There are residual peaks near the zero lag of the time series that can be ignored in the processing since these peaks are predictable from the length of the array. In this case the peaks occur between time zero and time 0.0074 s (twice the travel time of the length of the array due to the two stages of beamforming).

In these simulations, the cross-spectral density that was calculated is idealized and assumes an infinite averaging time. Long averaging is probably not practical for application as a survey tool since the integration times would need to be relatively short. The beamforming greatly assists the shortened averaging time with measured data by emphasizing the coherent part of the noise field coming from directly over the vertical array. As will be seen with the experimental data in the next section, with short averaging times the beamforming is critical to observing the bottom arrivals.

IV. EXPERIMENTAL RESULTS

Two measured data examples of the fathometer processing will be presented. The first example uses measured data of opportunity. The experiment had an active source (10 km from the receiver array) so the ambient noise was carefully windowed from the time series. This experiment had a fixed array with carefully measured array and water depths so it verifies the processing in a known environment. The second example is taken from a more practical scenario with the vertical array drifting over a varying bathymetry and sub-bottom. These arrays are both electronically quiet having electronic noise floor below sea-state zero.

A. Stellwagen Bank: ASCOT01

In 2001, the NATO Undersea Research Centre conducted the ASCOT-01 experiment near the Stellwagen Bank off the Northeast coast of the United States in a site with 101 m water depth.[16] This was primarily a geo-acoustic inversion experiment so sound sources were nearly continuously transmitting with the exception of about 0.5 s of data at the end of each file. Since the vertical array was fixed, these 0.5 s snapshots could be averaged over many snapshots producing, effectively, about a 30 s average. The sound source was located 10 km away and the ambient noise data was believed to be free from multipath and reverberation from the projector. The fixed and well measured geometry of ASCOT-01 provides a useful check of the bottom return timing.

A total of 33 elements with 0.5-m spacing array were used with the top hydrophone measured to be 52.25 m from the seabed. The frequency band considered is 200–1500 Hz. In Fig. 9, panel (a) shows the output after the first stage of beamforming. The bottom bounce is weak yet visible. From the single-phone correlations, the bottom returns were too weak to be visible without beamforming. In panel (b) of Fig. 9, the second stage of beamforming is applied and the bottom bounce is clearly visible. The peak near 0.07 s, in panel (b) puts the estimate of the distance to the bottom at 52.5 m, well within the experimental error on the measured hydrophone distance of 52.25 m. In this case, the array reference was the shallowest channel at 52.25 m which is near the midwater depth, and if a surface bounce were present, it would nearly interfere. To break the symmetry, the array beamforming was shifted to the deepest hydrophone and this is shown in panel (c) of Fig. 9. As predicted, in neither case is there evidence of a surface bounce. This may primarily be due to the beamforming deemphasize this return, but was
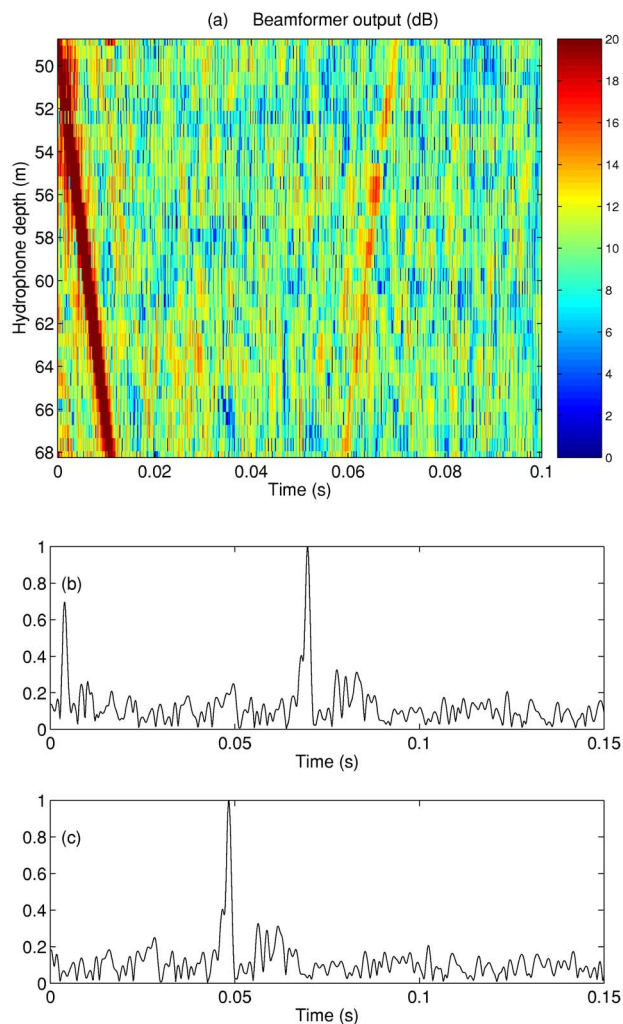

FIG. 9. Panel (a) shows the ASCOT-01 ambient noise processing after the first stage of beamforming. Near time zero, the direct arrival is visible arriving at later times as the wave front progresses down the array. In panel (b) is the second stage of beamforming showing the bottom bounce at around 0.07 s. Panel (c) shows the same processing with the array center shifted to the deepest hydrophone.

also seen to be weaker than might be expected from a true source as discussed previously. Sub-bottom returns are also present, but these could not be verified for correctness.

B. Strait of Sicily: Boundary 2003

The second experimental example is taken from a controlled set of (directional noise) data that were collected (by the second author) on a drifting array during the NATO Undersea Research Centres Boundary 2003 experiment. (This is the same data set as described in Ref. 3 where it was converted to sub-bottom layers by a different process.) The drifting array has 32 hydrophones spaced at 0.18 m (design frequency of 4.2 kHz). The wind varied during the experiment but was, on average, approximately 15 kn. The array was not equipped with a Global Positioning System receiver but was tracked using surface radar. At the time of the experiment, the depth of the array was not a critical factor and was therefore not measured carefully. However, it was reported that the hydrophones were to be kept less than about 80 m but
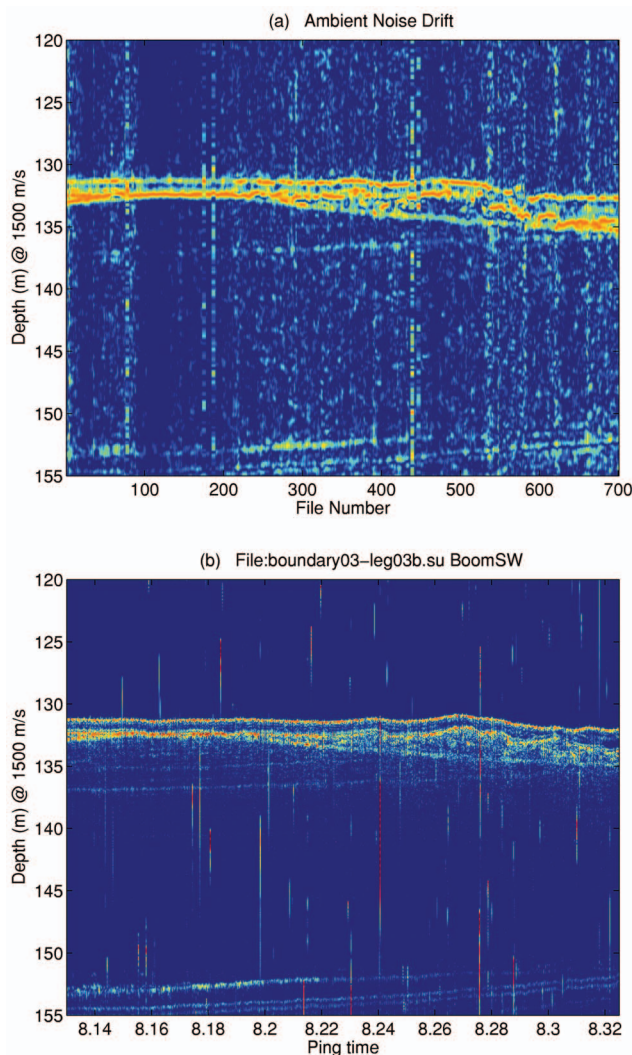
FIG. 10. In panel (a) the ambient noise fathometer processing is used and in panel (b) approximately the same track using a towed Uniboom sub-bottom profiler. The *y* axis is two-way travel times converted to depths using 1500 m/s sound speed.

some alignment of the ambient noise and Uniboom data were made with the data itself. The depth of the array was taken as 73.5 m for the entire track. The range of the array along the track was allowed to slide a few hundred meters. However, a single range correction was used for the entire track. There are features in both (a) and (b) that are similar as far down as 25 m into the seabed. The map of the bathymetry from the noise [panel (a)] also closely resembles that from the Uniboom survey.

V. SUMMARY AND CONCLUSIONS

Using the coherent components of the ocean ambient noise, a passive fathometer and seabed layer imaging technique has been described. In theory, this might be done with a single receiver, however this may require averaging times too long to be practical. Using a vertical array of receivers, beamforming on enfire was used to emphasize the coherent arrivals coming from directly above the array. Beamforming allows averaging the noise over a short time which then resembles random clicks coming from the surface. The processing technique has been illustrated with simulations, however, these simulations assumed infinite averaging time. Experimental data shows the processing also works with reasonable averaging times of about one minute. The first example showed a fixed array with carefully measured geometry and the bottom bounce path arriving at exactly the predicted time. The second example used a drifting array that showed both bathymetry and sub-bottom layering. A sub-bottom profiling sonar was taken along the same path as the drift to validate the results from the passive fathometer processing.

were probably between 70 and 80 m. The signals were sampled at 12 kHz and each channel was transformed to the frequency domain using 16384 point fast Fourier transforms (FFTs) (or around 1.4 s of data). Approximately 70 s of data were averaged to form the cross-spectral density and produce a single fathometer time trace (over the 50–4000 Hz frequency band).

Following the array drift, seismic reflection data were collected to image the sub-bottom layers. The seismic reflection data was collected by towing a Uniboom source (5813B seismic boomer) with a ten element towed array behind the NATO *R/V Alliance*. This sonar is designed to measure both the bathymetry and the strongest reflectors from the seabed. It was only possible to approximate the drifting array tracks with the Uniboom tracks.

In Fig. 10, the ambient noise [panel (a)] and Uniboom [panel (b)] processed data are shown. For these displays. the data envelope of the time series are taken and put on a decibel scale. There is a 12 dB dynamic range in the color scale. Since the array depth and position were not known exactly,

[1] C. H. Harrison and D. G. Simons, "Geoacoustic inversion of ambient noise: A simple method," J. Acoust. Soc. Am. **112**(4), 1377–1389 (2002).
[2] C. Harrison, "Sub-bottom profiling using ocean ambient noise," J. Acoust. Soc. Am. **115**(4), 1505–1515 (2004).
[3] C. Harrison, "Performance and limitations of spectral factorization for ambient noise sub-bottom profiling," J. Acoust. Soc. Am. **118**(5), 2913–2923 (2005).
[4] P. Roux, W. A. Kuperman and the NPAL Group, "Extracting coherent wave fronts from acoustic ambient noise in the ocean," J. Acoust. Soc. Am. **116**(4), 1195–2003 (2004).
[5] R. L. Weaver and O. I. Lobkis, "Ultrasonics without a source: Thermal fluctuation correlations at MHz frequencies," Phys. Rev. Lett. **87**, 134301 (2001).
[6] J. Rickett and J. Claerbout, "Acoustic daylight imaging via spectral factorization: Helioseismology and reservoir monitoring," Report 100, Stanford Exploration Project (unpublished).
[7] K. G. Sabra, P. Roux, and W. A. Kuperman, "Arrival-time structure of the time-averaged ambient noise cross-correlation function in an oceanic waveguide," J. Acoust. Soc. Am. **117**(1), 164–174 (2005).

[8]M. J. Buckingham, "A theoretical model of ambient noise in a low-loss shallow water channel," J. Acoust. Soc. Am. **67**(4), 1186–1192 (1980).

[9]C. H. Harrison, "Formulas for ambient noise level and coherence," J. Acoust. Soc. Am. **99**(4), 2055–2066 (1996).

[10]W. A. Kuperman and F. Ingenito, "Spatial correlation of surface generated noise in a stratified ocean," J. Acoust. Soc. Am. **67**(6), 1988–1996 (1980).

[11]F. B. Jensen, W. A. Kuperman, M. B. Porter, and H. Schmidt, *Computational Ocean Acoustics* (American Institute of Physics, Inc., New York, 1994).

[12]H. Schmidt, "SAFARI: Seismo-acoustic fast field algorithm for range independent environments. User's guide," SR-113, SACLANT Undersea Research Centre, La Spezia, Italy (unpublished).

[13]H. Schmidt and F. B. Jensen, "A full wave solution for propagation in multilayered viscoelastic media with application to Gaussian beam reflection at fluid-solid interfaces," J. Acoust. Soc. Am. **77**, 813–825 (1985).

[14]B. F. Cron and C. H. Sherman, "Spatial-correlation functions for various noise models," J. Acoust. Soc. Am. **34**, 1732–1736 (1962).

[15]H. Schmidt, "OASES version 3.1 user guide and reference manual," http://acoustics.mit.edu/faculty/henrik/oases.html, Department of Ocean Engineering Massachusetts Institute of Technology, Cambridge, MA (unpublished).

[16]J. Sellschopp, NATO Undersea Research Centre, Vaile S. Barolomeo 400, 19138 La Spezia, Italy, ASCOT-01, SACLANTCEN CD-ROM, 49, 2001.